

A magnetar parallax

H. Ding,^{1,2}★ A. T. Deller,^{1,2} M. E. Lower,^{1,3} C. Flynn,^{1,2} S. Chatterjee,⁴ W. Brisken,⁵
N. Hurley-Walker,⁶ F. Camilo,⁷ J. Sarkissian,⁸ V. Gupta^{1,2}

¹Centre for Astrophysics and Supercomputing, Swinburne University of Technology
John St, Hawthorn, VIC 3122, Australia

²ARC Centre of Excellence for Gravitational Wave Discovery (OzGrav)

³CSIRO Astronomy and Space Science, Australia Telescope National Facility, Epping, NSW 1710, Australia

⁴Cornell Center for Astrophysics and Planetary Science and Department of Astronomy, Cornell University, Ithaca, NY 14853, USA

⁵National Radio Astronomy Observatory, P.O. Box O, Socorro NM 87801, USA

⁶International Centre for Radio Astronomy Research, Curtin University, Bentley, WA 6102, Australia

⁷South African Radio Astronomy Observatory, 2 Fir Street, Observatory 7925, South Africa

⁸CSIRO Astronomy and Space Science, Parkes Observatory, PO Box 276, Parkes NSW 2870, Australia

Accepted XXX. Received YYY; in original form ZZZ

ABSTRACT

XTE J1810–197 was the first magnetar identified to emit radio pulses, and has been extensively studied during a radio-bright phase in 2003–2008. It is estimated to be relatively nearby compared to other Galactic magnetars, and provides a useful prototype for the physics of high magnetic fields, magnetar velocities, and the plausible connection to extragalactic fast radio bursts. Upon the re-brightening of the magnetar at radio wavelengths in late 2018, we resumed an astrometric campaign on XTE J1810–197 with the *Very Long Baseline Array*, and sampled 14 new positions of XTE J1810–197 over 1.3 years. The phase calibration for the new observations was performed with two phase calibrators that are quasi-colinear on the sky with XTE J1810–197, enabling substantial improvement of the resultant astrometric precision. Combining our new observations with two archival observations from 2006, we have refined the proper motion and reference position of the magnetar and have measured its annual geometric parallax, the first such measurement for a magnetar. The parallax of 0.40 ± 0.05 mas corresponds to a most probable distance $2.5^{+0.4}_{-0.3}$ kpc for XTE J1810–197. Our new astrometric results confirm an unremarkable transverse peculiar velocity of ≈ 200 km s^{−1} for XTE J1810–197, which is only at the average level among the pulsar population. The magnetar proper motion vector points back to the central region of a supernova remnant (SNR) at a compatible distance at ≈ 70 kyr ago, but a direct association is disfavored by the estimated SNR age of ~ 3 kyr.

Key words: radio continuum: transients – pulsars: individual: XTE J1810–197 – parallaxes – proper motions

1 INTRODUCTION

Magnetars are a class of highly magnetized, slowly rotating neutron stars (NSs) with surface magnetic field strengths typically inferred in the range 10^{14} – 10^{15} G, making them the most magnetic objects in the known universe. They have been observed to emit high energy electromagnetic radiation, and to undergo powerful X-ray and gamma-ray outbursts. The high energy emission from these objects is thought to be powered by the decay of their magnetic fields (Thompson & Duncan 1995) as opposed to dipole radiation for classical pulsars. To date, 29 magnetars and 6 magnetar candidates have been discovered (Olausen & Kaspi 2014)¹; however, only 6 magnetars have ever been observed to emit radio pulsations, partly due to a small birthrate for the class (Gill & Heyl 2007). SGR J1935+2154 recently joined the other 5 magnetars that have been observed to emit radio pulses. Its radio emission was detected in the form of an unprecedented radio pulse with a fluence of 1.5 ± 0.3 MJy ms (Andersen et al. 2020; Bochenek et al. 2020). That burst is the highest-fluence radio pulse ever recorded from

★ E-mail: haoding@swin.edu.au

¹ Catalogue: <http://www.physics.mcgill.ca/~pulsar/magnetar/main.html>

the Galaxy and confirms magnetars are plausible sources of extragalactic Fast Radio Bursts (FRBs). However, the mechanism by which such strong radio pulses are produced from magnetars is poorly understood (e.g. [Margalit et al. 2020](#)), as is the birth mechanism of magnetars.

Multi-wavelength observations of Galactic magnetars, including long-term timing and *Neutron Star Interior Composition Explorer* (NICER) observations, allow us to study the morphology and evolution of their magnetic fields, and potentially probe their internal structure ([Kaspi & Beloborodov 2017](#)). However, such studies are usually limited by the uncertainties in the underlying magnetar distances (and uncertain proper motions as well, in some cases). For instance, the X-ray spectrum fitting technique that has recently been made possible by observations with NICER requires a well-constrained, pre-determined distance to the target (which can be a magnetar) in order to infer its radius along with its mass ([Bogdanov et al. 2019](#)). Besides, owing to the enormous instability in spin-down rates (period derivative \dot{P}) of magnetars (e.g. [Camilo et al. 2007](#); [Archibald et al. 2015](#); [Scholz et al. 2017](#)), measuring the proper motion (not to mention parallax) via timing is difficult for magnetars; as such, using an accurate, *a priori* proper motion and parallax in the timing analysis of a magnetar can improve the reliability of the timing model, thus facilitating the study of long-term \dot{P} evolution. Furthermore, an accurate distance would enable unbiased estimation of the absolute flux of X-ray flares or the absolute fluence of giant radio pulses. On top of the studies focusing on the magnetars, accurate distance and proper motion for a magnetar also enables constraints to be placed on the distance to the dominant foreground (scattering) interstellar-medium (ISM) screen ([Putney & Stinebring 2006](#); see [Bower et al. 2014, 2015](#) for an example).

Proper motion measurements for magnetars are significant in their own right. Both the space velocities of neutron stars and their surface magnetic field strengths have been connected to the progenitor stellar masses and the processes of core-collapse supernovae. [Duncan & Thompson \(1992\)](#) suggested that the high magnetic fields of magnetars could be associated with very high space velocities of 10^3 km s^{-1} through e.g., asymmetric mass loss during core collapse or in the form of an anisotropic magnetized wind, or through a neutrino and/or photon rocket effect. Such processes would be ineffective for “ordinary” neutron star field strengths ($\lesssim 10^{13} \text{ G}$), leading to great interest in magnetar velocity estimates as diagnostics of their natal processes. So far the transverse velocity measurements that have been made (modulo large uncertainties) do not support a higher-than-average kick velocity for magnetars, with transverse velocities around the range of 200 km s^{-1} inferred for XTE J1810–197, PSR J1550–5418, and PSR J1745–2900 ([Helfand et al. 2007](#); [Deller et al. 2012](#); [Bower et al. 2015](#), respectively). Additionally, the proper motion of a magnetar could provide a crucial test of its association with nearby supernova remnants (SNR), especially when the magnetar is outside the SNR. More importantly, the proper motion enables us to infer the kinematic age of the magnetar as well as the SNR from the underlying association, which is more reliable than the characteristic age of either.

Both distance and proper motion for a magnetar can be geometrically measured with VLBI (very long baseline interferometry) astrometry at radio wavelengths. Observations of magnetar radio pulses reveal that they are quite distinct from the radio emission seen in pulsars – most of them have flat radio spectra and their pulse profiles are highly variable on timescales ranging from seconds to years. Radio emission from magnetars is also a relatively short-lived phenomenon, generally starting out bright after an outburst, then fading over the following months to years. After radio emission ceases, they then spend long periods of time in a radio-silent, quiescent state before the next outburst. With a current sample size of only 3 magnetars with precise VLBI proper motions, the (re-)appearance of a radio-emitting magnetar offers a valuable opportunity, particularly for pulsar timing and astrometry, both of which can be performed much more precisely with radio observations than with X-rays.

XTE J1810–197 (hereafter J1810) was discovered in 2003 due to an outburst at X-ray wavelengths ([Ibrahim et al. 2004](#)), and was subsequently seen to be pulsating at radio wavelengths with a period of 5.4 seconds ([Camilo et al. 2006](#)), the first time radio pulsations had been detected for a magnetar. During its brief period of radio brightness over a decade ago, two VLBA observations separated by 106 days were made, allowing the measurement of a proper motion of $13.5 \pm 1.0 \text{ mas yr}^{-1}$ – also the first for a magnetar ([Helfand et al. 2007](#)). The implied transverse velocity was $212 \pm 35 \text{ km s}^{-1}$ (assuming a distance of $3.5 \pm 0.5 \text{ kpc}$) and was the first indication that magnetar velocities might be much lower than the expectations outlined earlier in this section. J1810 subsequently faded into a 10 year quiescence at radio wavelengths until 2018 December 8, when it was found to be radio bright (and pulsating) again at Jodrell Bank ([Lyne et al. 2018](#)), Molonglo Radio Observatory ([Lower et al. 2018](#)) and Effelsberg ([Desvignes et al. 2018](#)). The flux density of the source ranged between 9 and 20 mJy from 835 MHz to 8 GHz, showing a flat spectrum.

Here we present new VLBI astrometric results for J1810 in Section 4, and lay out the direct indications of the results in Section 5. We also describe dual-calibrator phase calibration technique (also known as 1-D interpolation [Fomalont & Kopeikin 2003](#)) and detail the relevant data analysis in Sections 3 and 4. Throughout this paper, the uncertainties are provided at 68% confidence level unless otherwise stated.

2 OBSERVATIONS AND CORRELATION

After the re-activation of J1810 at radio wavelengths in December 2018, we observed the magnetar with the *Very Long Baseline Array* (VLBA) from January 2019 to November 2019 on a monthly basis (project code BD223). We re-visited J1810 with three consecutive VLBA observations in the same observing setup on 28 March, 6 April and 13 April 2020 (when J1810 was at its parallax maximum; project code BD231). Altogether there are 14 new VLBA observation epochs.

All the observations were carried out at around 5.7 GHz in astrometric phase referencing mode (where the pointing of the array alternates between the target and phase calibrator throughout the observation). Unlike typical astrometric observations, J1810 was phase-referenced to two phase calibrators: ICRF J175309.0-184338 ($4^{\circ}.1$ away from J1810, hereafter J1753) and VCS6 J1819-2036 ($2^{\circ}.5$ away from J1810,

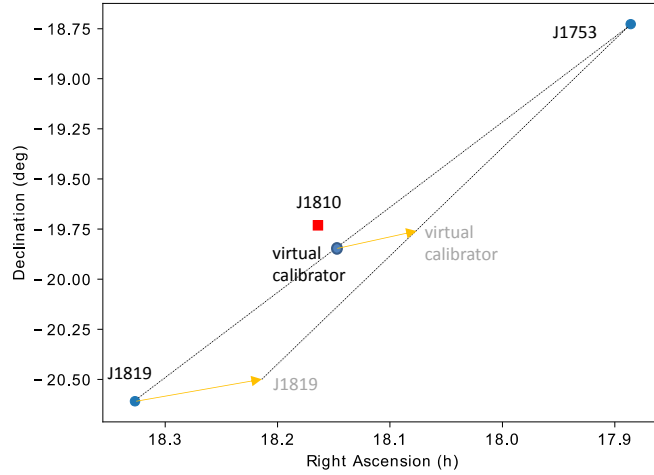


Figure 1. a) The diagram shows the positions of the magnetar (marked with red rectangle), the primary phase calibrator J1753 and secondary phase calibrator J1819. The virtual calibrator is chosen as the closest point (12.5 away) to J1810 on the J1753-to-J1819 geodesic line, which is at 62.43% of the distance to J1819 from J1753. **b)** Yellow arrows are overlaid on the calibrator plan to illustrate the discussion in Sections 4.2 and 4.4: if the position for J1819 was in error (greatly exaggerated here for visual effect – any position offset is in reality only at the ~ 1 mas level), the position of the virtual calibrator would change in the same direction. The degree of the position shift of the virtual calibrator would be 62.4% that of J1819. Any position error for J1753 would likewise affect the position of the virtual calibrator.

hereafter J1819), which are almost colinear with J1810 (see Figure 1). The purpose of this non-standard astrometric setup is explained in Section 3.1. ICRF J173302.7–130449 was observed as the fringe finder.

The data were correlated with the DiFX software correlator (Deller et al. 2011) in two passes, standard (ungated) and gated. For the gated pass, the off-pulse durations were excluded from the correlation in order to improve the signal-to-noise ratio (S/N) on the magnetar. For all the 14 observations, pulsar gating was applied based on the pulsar ephemerides obtained with our monitoring observations of the magnetar at the Parkes and Molonglo telescopes. The timing observations at Parkes were carried out under the project code P885; the relevant observing setup and data reduction are described in Lower et al. (in preparation). The timing observations at Molonglo were fulfilled as part of the UTMOST project (Jankowski et al. 2019; Lower et al. 2020).

Apart from the 14 new VLBA observations, we re-visited two archival VLBA observations of J1810 taken in 2006 under the project code BH142 and BH145A (Helfand et al. 2007). An overview of observation dates is provided in Figure 2. The two observations in 2006 were carried out at both 5 GHz and 8.4 GHz, using J1753 as the only phase calibrator. More details of the observing setup for the two observations in 2006 can be found in Helfand et al. (2007). Hereafter, where unambiguous, positions obtained from the two epochs in 2006 and the 14 new epochs are equally referred to, respectively, as the “year-2006 positions” and the “recent positions”.

3 DATA REDUCTION

All VLBI data were reduced with the `psrvlbireduce` (<https://github.com/dingswin/psrvlbireduce>) pipeline written in python-based `ParseITongue` (Kettenis et al. 2006). `ParseITongue` serves as an interface to interact with AIPS (Greisen 2003) and DIFMAP (Shepherd et al. 1994). The pipeline has been incrementally developed for VLBI pulsar observations over the last decade, notably for the large VLBA programs PSR π (Deller et al. 2019) and MSPSR π (e.g. Ding et al. 2020).

For the two year-2006 epochs, only data taken at 5 GHz were reduced and analyzed, in order to avoid potential position uncertainties due to any frequency-dependent core shift in the phase calibrators (e.g. Bartel et al. 1986; Lobanov 1998). All positions of J1810 were obtained from the gated J1810 data, the S/N of which exceeded the ungated J1810 data by 40% on average.

Due to multi-path scattering caused by the turbulent ISM along the line of sight to J1810 or J1819, the deconvolved angular size of J1810 is mildly broadened by 0.7 ± 0.4 mas (detailed in Appendix A), and J1810 (as well as J1819) is fainter at longer baselines. In addition, J1819 exhibits intrinsic source structure, with a jet-like feature extending over ~ 10 mas. Accordingly, J1819 is heavily resolved by the longest baselines of the VLBA, with a flux density of at most a couple of mJy on baselines longer than 50 M λ (mega-wavelength). The three stations furthest from the geographic centre of VLBA are MK (Mauna Kea), SC (St. Croix) and HN (Hancock), each of which only has 0–1 baselines shorter than 50 M λ . Unsurprisingly, we found that while valid solutions could still often be found, the phase solutions for HN, MK, and SC are much noisier than for the remainder of the array. On top of this, atmospheric fluctuation causes larger phase variation at longer baselines, which, combined with the worse phase solutions, makes phase wraps (to be explained in Section 3.1) at MK, SC and HN hard to determine.

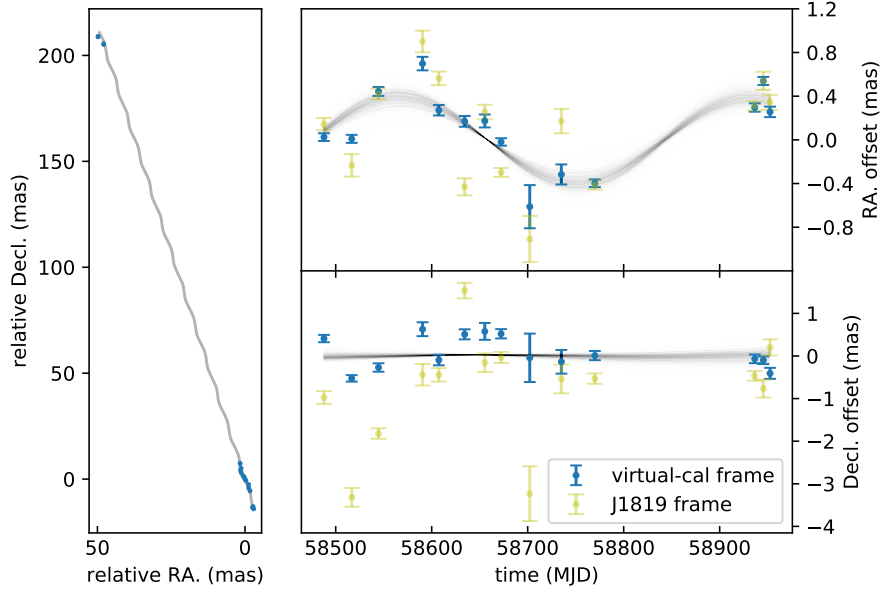


Figure 2. **Left panel:** position evolution of J1810 relative to $18^{\text{h}}09^{\text{m}}51^{\text{s}}.08333, -19^{\circ}43'52''.1398$ from 2006 to 2020. **Right panel:** recent positions of J1810 with proper motion subtracted measured in the virtual-calibrator frame (blue) and J1819 frame (yellow; see Section 4.1 for explanations of different reference frames); to convenience visual comparison, the two sets of positions adopt the same systematic uncertainties at each epoch as obtained in the virtual-calibrator frame. Overlaid are the best-fit models for 500 bootstrap draws from the positions measured in the virtual-calibrator frame. Here, the systematic uncertainties for the positions measured in the virtual-calibrator frame are still under-estimated, which is addressed in Section 4.3 using a bootstrap technique. Obviously, the positions measured in the virtual-calibrator frame provide tighter constraints to the model.

We found that the image S/N for J1810 generally improves when MK, SC and HN are excluded from the target field data, and as a result, taking the three stations out of the J1810 data leads to a statistical positional error comparable to that obtained when using the full array. Therefore, we consistently flagged the three stations from the final J1810 data for 14 recent epochs. However, we did not remove the three stations from any calibration steps, because we found the participation of the three stations allows better performance of self-calibration on J1819 at other stations.

The applied calibration steps in this work are largely the same as the PSR π project (Deller et al. 2019) except for the phase calibration. For the two year-2006 epochs, the phase solutions obtained with J1753 were directly transferred to J1810; whereas, for the recent 14 epochs, phase solutions were corrected based on the positions of J1753 and J1819, before being applied to J1810. Such a technique, though previously adopted by other researchers (e.g. Fomalont & Kopeikin 2003), is applied to a pulsar for the first time.

3.1 Dual-calibrator phase calibration

During the phase calibration of VLBI data, the calibration step k ($k = 2, 3, \dots$) provides an increment of the phase difference $\Delta\phi_n^{(k)}(t)$ between the station n and the reference station in the VLBI array at a given time t (for simplicity, frequency-dependency is not accounted for), which is then added to the previous sum of the phase difference $\phi_n^{(k-1)}(t)$ when the new solutions are applied. The phase calibration of the primary phase calibrator (J1753 for this work) is followed by the self-calibration of the secondary phase calibrator (J1819 for this work), the phase solutions of which are predominantly limited by anisotropic atmospheric (including ionosphere and troposphere) propagation effect. Accordingly, the position-dependent phase difference should be formulated as $\Delta\phi_n(\vec{x}, t)$, where \vec{x} represents the 2-D sky position. In the normal phase calibration, the solutions $\Delta\phi_n(\vec{x}_S, t)$ obtained with the self-calibration of the secondary phase calibrator at \vec{x}_S are directly given to the target. The closer \vec{x}_S is to the target field, the better $\Delta\phi_n(\vec{x}_S, t)$ can approximate the unknown $\Delta\phi_n(\vec{x}_T, t)$ at the target field. In cases where \vec{x}_S is $\gtrsim 1^\circ$ away from the target field, considerable offsets are expected between $\Delta\phi_n(\vec{x}_S, t)$ and $\Delta\phi_n(\vec{x}_T, t)$ (especially at lower frequencies), which are commonly treated as systematic errors when using the normal phase calibration. However, if the primary phase calibrator, secondary phase calibrator and the target happen to be quasi-colinear on the sky, $\Delta\phi_n(\vec{x}_T, t)$ can be well approximated by phase solutions corrected from $\Delta\phi_n(\vec{x}_S, t)$ (Fomalont & Kopeikin 2003).

It is easy to prove that for three arbitrary different co-linear positions \vec{x} , \vec{x}_1 and \vec{x}_2 ,

$$\phi_n(\vec{x}, t) = \frac{\vec{x}_1 - \vec{x}}{\vec{x}_1 - \vec{x}_2} \phi_n(\vec{x}_2, t) + \frac{\vec{x} - \vec{x}_2}{\vec{x}_1 - \vec{x}_2} \phi_n(\vec{x}_1, t), \quad (1)$$

assuming higher-than-first-order terms are negligible (as supported by Chatterjee et al. 2004; Kirsten et al. 2015). Specific to the self-calibration

of the secondary phase calibrator, we have $\Delta\phi_n(\vec{x}, t) = \Delta\phi_n(\vec{x}_S, t) \cdot (\vec{x}_P - \vec{x}) / (\vec{x}_P - \vec{x}_S)$, where \vec{x}_P and \vec{x}_S refer to the position of the primary phase calibrator and secondary phase calibrator, respectively; this relation allows us to extrapolate to $\Delta\phi_n(\vec{x}, t)$ at any position \vec{x} colinear with J1753 and J1819 based on $\Delta\phi_n(\vec{x}_{J1819}, t)$.

We calculated the closest position to J1810 on the J1753-to-J1819 geodesic line (an arc), where it can best approximate $\Delta\phi_n(\vec{x}_{J1810}, t)$. Since it acts like a phase calibrator for J1810, hereafter we term it the “virtual calibrator” for J1810. The position of the virtual calibrator is $\vec{x}_v = 0.38 \cdot \vec{x}_{J1753} + 0.62 \cdot \vec{x}_{J1819}$, which is 12.5 away from J1810 (see Figure 1). Accordingly, the phase solutions extrapolated to the virtual calibrator are $\Delta\phi_n(\vec{x}_v, t) = 0.62 \cdot \Delta\phi_n(\vec{x}_{J1819}, t)$; using this relation, we corrected the phase solutions of J1819 obtained with its self-calibration. The correction was implemented with a dedicated module called `calibrate_target_phase_with_two_colinear_phscals` that was newly added to the `vlbatasks.py`, as a part of the `psrvlbireduce` package. One of the functions of the module is to solve the phase ambiguity of $\Delta\phi_n(\vec{x}_{J1819}, t)$ prior to multiplying $\Delta\phi_n(\vec{x}_{J1819}, t)$ by 0.62.

The biggest challenge of the dual-calibrator phase calibration is the phase ambiguity of $\Delta\phi_n(\vec{x}_{J1819}, t)$, which can be equivalently expressed as $\Delta\phi_n(\vec{x}_{J1819}, t) \pm 2i\pi$ ($i = 0, 1, 2, \dots$). This phase ambiguity will not change the quality of solutions for the normal phase calibration, but will cause trouble for the dual-calibrator phase calibration, as the periodicity of the phase is broken when multiplied by a factor. The degree of phase ambiguity depends on observing frequency and angular distance between the main and secondary phase calibrator; for this work (5.7 GHz, 6.5°), we run into mild phase ambiguity, mainly at the longest baselines (that we do not use anyway as mentioned earlier in this section). Among the recent epochs, the smallest size of the synthesized beam excluding MK, SC and HN is 2.9×8.2 mas, more than two times larger than the level of the systematic uncertainties dominated by propagation effect (see Figure 2). Therefore, for this work, we consider $\Delta\phi_n(\vec{x}_{J1819}, t)$ less likely to turn more than one wrap, and impossible to turn more than two wraps (i.e. $|i| \leq 2$).

We resolved the phase ambiguity of $\Delta\phi_n(\vec{x}_{J1819}, t)$ in a semi-automatic and iterative manner. The pipeline would go through all values of $\Delta\phi_n(\vec{x}_{J1819}, t)$ at each station. If $|\Delta\phi_n(\vec{x}_{J1819}, t)| < \pi/2$ holds true throughout the observation, then the solutions $\Delta\phi_n(\vec{x}_{J1819}, t)$ are deemed phase-unambiguous, and no human intervention is needed for the station n . Otherwise, $\Delta\phi_n(\vec{x}_{J1819}, t)$ solutions are plotted out for inspection and interactive correction. In most cases, no interactive correction is necessary after the inspection of the $\Delta\phi_n(\vec{x}_{J1819}, t)$ plot, as the solutions look continuous, oscillating around 0 within a reasonable range (e.g. between $\pm 2\pi/3$). In the few cases where interactive corrections are needed, solutions are ambiguous in phase for at most 1 or 2 stations per observation. This enabled us to take a simple, brute-force approach to trialing the plausible possibilities for phase wraps (adding or subtracting an integer multiple by 2π radians to the solution) with interactive correction. For every possibility, we implemented the dual-calibrator phase calibration using the resultant solution and ran through the complete (data-reduction and imaging) pipeline. The correct $\Delta\phi_n(\vec{x}_v, t)$ should outperform other possibilities in terms of the image S/N for J1810 (and the S/N difference is normally significant), as it better approximates the $\Delta\phi_n(\vec{x}_{J1810}, t)$. This S/N criterium helps us find the “real” $\Delta\phi_n(\vec{x}_{J1819}, t)$, thus the right $\Delta\phi_n(\vec{x}_v, t)$. The obtained solutions $\Delta\phi_n(\vec{x}_v, t)$ were then transferred to J1810.

More generally, if no phase-calibrator pair quasi-colinear with the target is found, one can extrapolate to $\Delta\phi_n(\vec{x}, t)$ at any position \vec{x} with three non-colinear phase calibrators (also known as 2-D interpolation, Fomalont & Kopeikin 2003; Rioja et al. 2017). Despite the longer observing cycle and hence sparser time-domain sampling (unless using the multi-view observing setup, Rioja et al. 2017), the tri-calibrator phase calibration can in principle remove all the first-order position-dependent systematics.

4 SYSTEMATIC ERRORS AND ASTROMETRIC FITS

4.1 Reference frames in relative VLBI astrometry

Similar to the way a reference frame is normally defined in non-relativistic (Cartesian) contexts, a reference frame in the context of relative VLBI astrometry (hereafter reference frame or frame) generally refers to a system of an infinite amount of sky positions that are tied to a phase calibrator (not necessarily a real one), in which positions are measured relative to the phase calibrator. In this work there are three different reference frames where we can measure the positions of J1810: the J1753 frame, the J1819 frame, and the virtual-calibrator frame. To be more specific, in the J1753/J1819 frame, the positions are measured relative to the brightest spot of the model image for J1753/J1819 respectively. By applying an identical model of J1753/J1819² during the fringe fitting and self-calibration steps, the J1753/J1819 images at different epochs are aligned, respectively, to $17^{\text{h}}53^{\text{m}}09^{\text{s}}.0886$, $-18^{\circ}43'38''.520$ and $18^{\text{h}}19^{\text{m}}36^{\text{s}}.8955$, $-20^{\circ}36'31''.573$; the virtual-calibrator frame is thus anchored to $18^{\text{h}}09^{\text{m}}35^{\text{s}}.9437$, $-19^{\circ}55'49''.656$, determined by the relation $\vec{x}_v = 0.38 \cdot \vec{x}_{J1753} + 0.62 \cdot \vec{x}_{J1819}$. For the 14 recent epochs, the final positions of J1810 were measured in the virtual-calibrator frame, though the positions of J1810 were also measured in the other two frames for various purposes (see Section 4.2 and Figure 2). The two year-2006 positions were merely measured in the J1753 frame, as J1753 is the only available phase calibrator for these observations.

4.2 Systematic errors and frame transformation

Similar to the way in which systematic positional errors for pulsars in the PSR π project were evaluated using Eqn 1 of Deller et al. (2019) to account for both differential ionospheric propagation effects and thermal noise at secondary phase calibrators, the estimation of systematic

² available at <https://data-portal.hpc.swin.edu.au/dataset/calibrator-models-used-for-vlba-astrometry-of-xte-j1810-197>

uncertainty for the measured positions of J1810 is based on the mathematical formalism

$$\Delta_{\text{sys}}^2 = \left(A \cdot \frac{s}{1 \text{ arcmin}} \cdot \overline{\text{csc } \epsilon} \right)^2 + (B/S)^2, \quad (2)$$

where Δ_{sys} is the ratio of the systematic error to the synthesized beam size, ϵ stands for elevation angle, $\overline{\text{csc } \epsilon}$ is the average $\text{csc } \epsilon$ for a given observation (over time and antennas), s is the angular separation between J1810 and the calibrator of the frame, S represents the image S/N of the calibrator of the frame, and A and B are coefficients to be determined. However, unlike Eqn 1 of Deller et al. (2019), in Eqn 2 the two contributing terms on the right side are added in quadrature. Given that they should be uncorrelated, this is more appropriate than the linear summation in Eqn 1 of Deller et al. (2019).

For this work, the second term of Eqn 2 is negligible for any of the three frames, as both J1753 and J1819 are strong sources, with a brightness $\geq 24 \text{ mJy beam}^{-1}$ at our typical resolution (after MK, SC and HN have been removed from the array). In order to find a reasonable estimate of A for this work, we measured the positions of J1810 consistently in the J1753 frame for all 16 epochs, and determined the value of A that renders an astrometric fit (see ‘‘direct fitting’’ in Section 4.3) with unity reduced chi-square, or $\chi^2_{\nu} = 1$. We obtained $A = 3 \times 10^{-4}$. We note that, in principle, A is invariant with respect to different reference frames. As is mentioned in Section 4.1, the final positions of J1810 were measured in the virtual-calibrator frame for the 14 recent epochs and in the J1753 frame for the two year-2006 epochs. Using $A = 3 \times 10^{-4}$ and Eqn 2 without the second term, we acquired systematic errors for each epoch, which was then added in quadrature to the random errors.

After the determination of the systematic errors, the next step is to transform positions into the same reference frame. Since J1753 and J1819 are remote quasars almost static in the sky, the frame transformation is simply translational. We translated the two year-2006 positions measured from the J1753 to the virtual-calibrator frame. The translation is equivalent, but in the reverse direction, to translate from the virtual-calibrator frame to the J1753 frame, which is easier to comprehend. In order to translate the virtual-calibrator frame to the J1753 frame, the position of the virtual calibrator needs to be measured in the J1753 frame, which can be accomplished by measuring the position of J1819 in the J1753 frame. The method to estimate the position of J1819 \vec{x}'_{J1819} and its uncertainty $\vec{\sigma}'_{\text{J1819}}$ in the J1753 frame is detailed in Section 3.2 of Ding et al. (2020).

As is shown in Figure 1, once \vec{x}'_{J1819} is measured in the J1753 frame, the new position of the virtual calibrator \vec{x}'_{v} in the J1753 frame is also determined, the uncertainty $\vec{\sigma}'_{\text{v}}$ of which is 0.62 times $\vec{\sigma}'_{\text{J1819}}$. The difference between \vec{x}'_{v} and \vec{x}_{v} (or 0.62 times the difference between \vec{x}'_{J1819} and \vec{x}_{J1819}) was used to translate the two year-2006 positions of J1810 from the J1753 frame to the virtual-calibrator frame. The $\vec{\sigma}'_{\text{v}}$ was added in quadrature to the error budget (already including systematic and random errors) of the two year-2006 positions.

4.3 Proper motion, parallax and distance

After including the systematic errors and unifying to the virtual-calibrator frame, the 16 positions of J1810 can be used for astrometric fitting. Astrometric fitting was performed using `pmpar`³. The median among the 16 epochs, MJD 58645, was adopted as the reference epoch. The results out of direct fitting are reproduced in Table 1, the χ^2_{ν} of which is 10.6. The large χ^2_{ν} suggests the systematic errors for the recent 14 positions are probably under-estimated, and the actual uncertainty for either parallax or proper motion is about 3 times larger than the uncertainty from direct fitting.

Applying a bootstrap technique to astrometry can generally provide more conservative uncertainties, compared to direct fitting (e.g. Deller et al. 2019). In the same way as is described in Section 3.1 on Ding et al. (2020), we bootstrapped 100000 times, from which we assembled 100000 fitted parallaxes, proper motions and reference positions for J1810. The marginalized histograms for parallax and proper motion as well as their paired error ‘‘ellipses’’ are displayed in Figure 3. We reported the most probable value at the peak of each histogram as the measured value; the most compact interval containing 68% of the sample was taken as the 68% uncertainty range of the measured value (see Figure 3). The parallax and proper motion estimated with bootstrap are listed in Table 1, which are highly consistent with direct fitting while over 3 times more conservative (as is expected from the χ^2_{ν} of direct fitting). Thus, the precision achieved for parallax and proper motion gauged with bootstrap can be deemed reasonable. The parallax corresponds to the distance $2.5^{+0.4}_{-0.3} \text{ kpc}$. Such a precision in distance would not be achieved with normal phase calibration using the same data (see Figure 2).

4.4 Absolute position

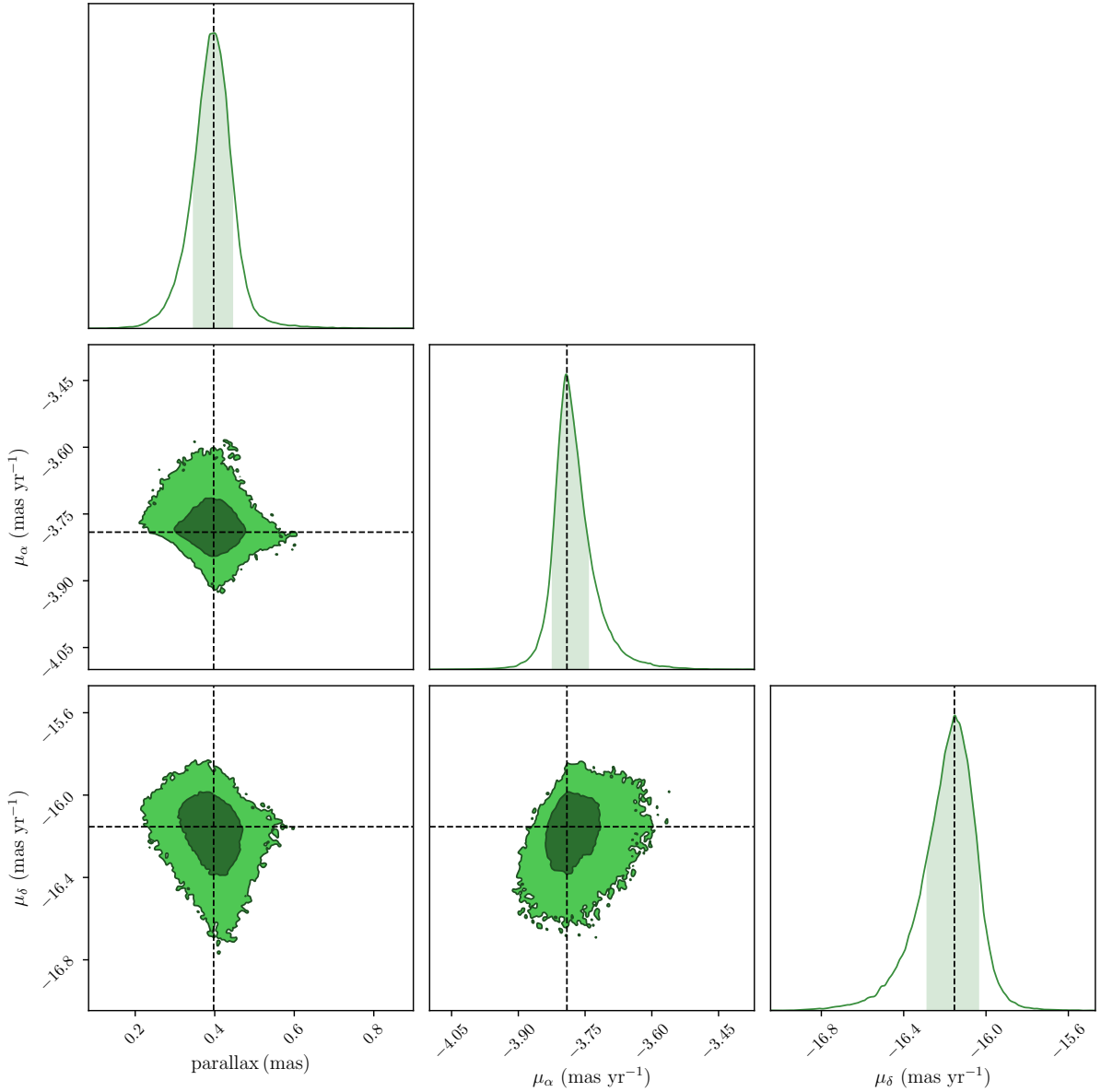
Along with proper motion and parallax, a reference position $18^{\text{h}}09^{\text{m}}51^{\text{s}}.083326 \pm 0.03 \text{ mas}$, $-19^{\circ}43'52''.1398 \pm 0.1 \text{ mas}$ at the reference epoch MJD 58645 was also obtained for J1810 with bootstrap. We note again the reference position was measured in the virtual-calibrator frame. According to the relation $\vec{x}_{\text{v}} = 0.38 \cdot \vec{x}_{\text{J1753}} + 0.62 \cdot \vec{x}_{\text{J1819}}$, change in \vec{x}_{J1753} or \vec{x}_{J1819} would cause the position shift of the virtual calibrator $\Delta \vec{x}_{\text{v}}$ (hence the position of J1810), following the relation

$$\Delta \vec{x}_{\text{v}} = 0.38 \cdot \Delta \vec{x}_{\text{J1753}} + 0.62 \cdot \Delta \vec{x}_{\text{J1819}}. \quad (3)$$

³ <https://github.com/walterfb/pmpar>

Table 1. Proper motion and distance measurements for J1810

method	$\mu_\alpha \equiv \dot{\alpha} \cos \delta$ (mas yr ⁻¹)	μ_δ (mas yr ⁻¹)	ϖ (mas)	D (kpc)	References
direct fitting	-3.78 ± 0.01	-16.18 ± 0.03	0.39 ± 0.01	2.5 ± 0.1	this work
bootstrap	$-3.79^{+0.05}_{-0.03}$	-16.2 ± 0.1	0.40 ± 0.05	$2.5^{+0.4}_{-0.3}$	this work
Previous VLBI astrometry	-6.60 ± 0.06	-11.72 ± 1.03	–	–	Helfand et al. (2007)
red clump stars	–	–	–	3.1 ± 0.5	Durant & van Kerkwijk (2006)
neutral hydrogen absorption	–	–	–	3.1–4.0	Minter et al. (2008)


Figure 3. Error “ellipses” and marginalized histograms for parallax and proper motion. In each histogram, the dashed line marks the measured value; the shade stands for the 68% confidence interval. In each error “ellipse”, the dark and bright contour enclose, respectively, 68% and 95% of the bootstrapped data points.

Using Eqn 3 and the method outlined in Section 3.2 on Ding et al. (2020), the reference position was shifted to align with the latest positions of J1753 and J1819⁴. The shifted reference position $18^{\text{h}}09^{\text{m}}51^{\text{s}}.08333 \pm 0.3 \text{ mas}$, $-19^{\circ}43'52''.1418 \pm 0.5 \text{ mas}$ is the absolute position of J1810 at MJD 58645, where the uncertainties of the J1753 and J1819 positions have been propagated onto the uncertainty budget. At 5.7 GHz, the effect of frequency-dependent core shift (e.g. Bartel et al. 1986; Lobanov 1998) is at the $\lesssim 0.1 \text{ mas}$ level in each direction (Sokolovsky et al. 2011), which makes unnoticeable difference to the uncertainty of the absolute position.

5 DISCUSSION

As is shown in Table 1, our new proper motion significantly improves on the previous value inferred from the two year-2006 positions; the new distance $D = 2.5^{+0.4}_{-0.3} \text{ kpc}$ is consistent with $3.1 \pm 0.5 \text{ kpc}$ estimated using red clump stars (Durant & van Kerkwijk 2006), while in mild tension with $3.1\text{--}4.0 \text{ kpc}$ constrained with neutral-hydrogen absorption (Minter et al. 2008), suggesting the distance to the neutral-hydrogen screen was over-estimated.

In models of NS kicks from the electromagnetic rocket effect (Harrison & Tademaru 1975) one might expect magnetars to have higher velocities (Duncan & Thompson 1992). Our new parallax and proper motion corresponds to the transverse velocity $v_t = 198^{+29}_{-23} \text{ km s}^{-1}$. Using the Galactic geometric parameters provided by Reid et al. (2019) and assuming a flat rotation curve between J1810 and the Sun, the peculiar velocity (with respect to the neighbourhood of J1810) perpendicular to the line of sight was calculated to be $v_b = -54 \pm 8 \text{ km s}^{-1}$ and $v_l = -175 \pm 26 \text{ km s}^{-1}$. Our refined astrometric results consolidate the conclusion by Helfand et al. (2007) that J1810 has a peculiar velocity typically seen in “normal” pulsars, unless its radial velocity is several times larger than the transverse velocity.

5.1 SNR Association

The closest cataloged SNR to J1810 is G11.0–0.0 (Green 2019)⁵, a partial-shell SNR $9' \times 11'$ in size (Brogan et al. 2004, 2006). The position of its geometric center is $18^{\text{h}}10^{\text{m}}04^{\text{s}}$, $-19^{\circ}25'$, $19'$ away from J1810. The latest distance estimate of G11.0–0.0 by Shan et al. (2018) is $2.4 \pm 0.7 \text{ kpc}$, consistent with our new distance of J1810. Using our astrometric results, we find that the projected position at 70 kyr ago is $18^{\text{h}}10^{\text{m}}09^{\text{s}}.8$, $-19^{\circ}25'00''$, about $1'$ east to the geometric center of G11.0–0.0. For the above geometric reasons, it is possible that J1810 is associated with G11.0–0.0.

The plausibility of this potential association can be tested by considering the ages of both J1810 and G11.0–0.0. The spin-down rate \dot{P} is erratic for J1810 (Camilo et al. 2007) as well as other magnetars (Archibald et al. 2015; Scholz et al. 2017), making the characteristic age τ_c an unreliable estimate of the true age for J1810. Over the course of a decade, the changing value of \dot{P} for J1810 has led to the τ_c ($\propto 1/\dot{P}$) increasing from 11 kyr (Camilo et al. 2007) to 31 kyr (Pintore et al. 2018). While the characteristic age is currently less than the tentative kinematic age τ_k^* that the tentative association would imply, the unreliability of the τ_c estimator in the case of magnetars suggests that the association cannot be ruled out on this basis.

From the perspective of G11.0–0.0, the compactness of the SNR (see Figure 1 of Castelletti et al. 2016) suggests that it is probably in the Sedov-Taylor stage. In this stage, the relation between the SNR radius R_{SNR} and its age τ_{SNR} can be rewritten from Sedov (1959) as

$$R_{\text{SNR}} \approx 5 \left(\frac{E}{10^{51} \text{ erg}} \right)^{1/5} \left(\frac{n}{30 \text{ cm}^{-3}} \right)^{-1/5} \left(\frac{\tau_{\text{SNR}}}{1 \text{ kyr}} \right)^{2/5} \text{ pc}, \quad (4)$$

where the injected energy E is expressed in a value typical of spherical SNRs expanding into the Galactic ISM, and the ambient ISM density $n \sim 30 \text{ cm}^{-3}$ for the γ -ray-emitting region including G11.0–0.0 was required to power the observed γ -ray emission above 1 TeV at a distance of 2.4 kpc (Castelletti et al. 2016). At an SNR distance $D_{\text{SNR}} = 2.4 \text{ kpc}$ (Shan et al. 2018), $R_{\text{SNR}} \leq 3.8 \text{ pc}$ (corresponding to the angular size along the long axis), which yields $\tau_{\text{SNR}} \lesssim 3 \text{ kyr}$ using Eqn 4, consistent with an SNR in the early part of the Sedov-Taylor phase. A τ_{SNR} of 70 kyr can be made possible with an injected energy 500 times smaller than the typically-assumed value of 10^{51} erg , which is extremely unlikely (Leahy 2017). Therefore, we conclude G11.0–0.0 is not directly associated with J1810. This is not too surprising, as less than half of the known magnetar population has a potential SNR association (Olausen & Kaspi 2014). Additionally, it has been proposed a strong post-birth magnetar wind can accelerate the dissipation of the SNR (Duncan & Thompson 1992).

Though G11.0–0.0 is not directly associated with J1810, the 3-D geometric alignment might not be a coincidence. One explanation for the geometric alignment is: the progenitor star of J1810 has been in orbit with another supergiant companion; and G11.0–0.0 is the SNR for the “divorced” companion of J1810. In such a scenario, the progenitor of J1810 underwent a supernova explosion $\approx 70 \text{ kyr}$ ago and became unbound from its original companion. The companion star continued evolving in isolation before itself undergoing a supernova explosion at $\lesssim 3 \text{ kyr}$ ago. In this “companion SNR” scenario, assuming the components of the stellar system were formed at approximately the same time, the progenitor of J1810 should be slightly more massive than its companion (and hence evolve faster). However, given that this scenario would require that the companion underwent a supernova explosion only $\approx 67 \text{ kyr}$ (compared to the typical supergiant age of $\gtrsim 1 \text{ Myr}$) after the first supernova, the mass difference of the two progenitor stars would have to be small.

⁴ http://astrogeo.org/vlbi/solutions/rfc_2020b/rfc_2020b_cat.html

⁵ <http://www.mrao.cam.ac.uk/surveys/snrs/>

Assuming no peculiar velocity of the progenitor binary system (with regard to its neighbourhood mean) as well as a flat rotation curve between the Sun and J1810, the expected proper motion of the barycentre of the supergiant binary as observed from the Earth is only 1.2 mas yr^{-1} . The additional proper motion of the companion due to the orbital motion at the moment of unbinding is even smaller for supergiant binaries. Thus, the accumulated position shift of the companion star after the unbinding is at the $1.3'$ level across 67 kyr, which does not violate the premise of the “companion SNR” scenario.

In principle, given the large age scatter of supergiants, the “companion SNR” scenario allows J1810 to be indirectly associated with an SNR further away. For example, J1810 can be traced back to $17'$ west to the centre of SNR G11.4–0.1 (which is though far from the boundary of the SNR) at ≈ 144 kyr ago. However, the relatively small characteristic age $\tau_c = 11\text{--}31$ kyr favors the closer indirect association (or no association) with G11.0–0.0. Despite the “companion SNR” scenario, we note that it is highly possible that J1810 does not come from the G11.0–0.0 region; instead, it comes from an already dissipated SNR between J1810 and G11.0–0.0 (as supported by [Duncan & Thompson 1992](#)). Longer-term τ_c monitoring with timing observations on J1810 will offer a more credible range of τ_c to be compared with the tentative kinematic age $\tau_k^* \approx 70$ kyr suggested by the possible “indirect” association between G11.0–0.0 and J1810. Besides, a deeper search for SNR in the narrow region between J1810 and G11.0–0.0 might provide an alternative candidate for the SNR associated with J1810.

ACKNOWLEDGEMENTS

We thank Marten van Kerkwijk for his in-depth review and helpful comments on this paper. H.D. is supported by the ACAMAR (Australia-China Consortium for Astrophysical Research) scholarship, which is partly funded by the China Scholarship Council (CSC). A.T.D. is the recipient of an ARC Future Fellowship (FT150100415). S.C. acknowledges support from the National Science Foundation (AAG 1815242). Parts of this research were conducted by the Australian Research Council Centre of Excellence for Gravitational Wave Discovery (OzGrav), through project number CE170100004. This work is based on observations with the Very Long Baseline Array (VLBA), which is operated by the National Radio Astronomy Observatory (NRAO). The NRAO is a facility of the National Science Foundation operated under cooperative agreement by Associated Universities, Inc. Data reduction and analysis was performed on OzSTAR, the Swinburne-based supercomputer. This work made use of the Swinburne University of Technology software correlator, developed as part of the Australian Major National Research Facilities Programme and operated under license.

DATA AND CODE AVAILABILITY

The pipeline for data reduction is available at <https://github.com/dingswin/psrvlbireduce>.

All VLBA data used in this work can be found at <https://archive.nrao.edu/archive/advquery.jsp> under the project codes bd223, bd231, bh142 and bh145a. The calibrator models for J1753 and J1819 can be downloaded from

<https://data-portal.hpc.swin.edu.au/dataset/calibrator-models-used-for-vlba-astrometry-of-xte-j1810-197>.

REFERENCES

- Andersen B., et al., 2020, arXiv preprint arXiv:2005.10324
 Archibald R., Kaspi V., Ng C.-Y., Scholz P., Beardmore A., Gehrels N., Kennea J. A., 2015, *ApJ*, 800, 33
 Bartel N., Herring T. A., Ratner M. I., Shapiro I. I., Corey B. E., 1986, *Nature*, 319, 733
 Bochenek C., Ravi V., Belov K., Hallinan G., 2020, arXiv preprint arXiv:2005.10828
 Bogdanov S., et al., 2019, *ApJ*, 887, L25
 Bower G. C., et al., 2014, *ApJ*, 780, L2
 Bower G. C., et al., 2015, *ApJ*, 798, 120
 Brogan C. L., Devine K., Lazio T., Kassim N., Tam C., Brisken W. F., Dyer K., Roberts M., 2004, *AJ*, 127, 355
 Brogan C. L., Gelfand J., Gaensler B., Kassim N., Lazio T., 2006, *ApJ*, 639, L25
 Camilo F., Ransom S. M., Halpern J. P., Reynolds J., Helfand D. J., Zimmerman N., Sarkissian J., 2006, *Nature*, 442, 892
 Camilo F., et al., 2007, *ApJ*, 663, 497
 Castelletti G., Giacani E., Petriella A., 2016, *A&A*, 587, A71
 Chatterjee S., Cordes J., Vlemmings W., Arzoumanian Z., Goss W., Lazio T., 2004, *ApJ*, 604, 339
 Deller A. T., et al., 2011, *PASP*, 123, 275
 Deller A. T., et al., 2012, *ApJ*, 756, L25
 Deller A. T., et al., 2019, *ApJ*, 875, 100
 Desvignes G., et al., 2018, *ATel*, 12285
 Ding H., Deller A. T., Freire P., Kaplan D. L., Lazio T. J. W., Shannon R., Stappers B., 2020, *ApJ*, 896, 85
 Duncan R. C., Thompson C., 1992, *ApJ*, 392, L9
 Durant M., van Kerkwijk M. H., 2006, *ApJ*, 650, 1070
 Fomalont E. B., Kopeikin S. M., 2003, *ApJ*, 598, 704
 Gill R., Heyl J., 2007, *MNRAS*, 381, 52
 Green D., 2019, *Journal of Astrophysics and Astronomy*, 40, 36

- Greisen E. W., 2003, in Heck A., ed., *Astrophysics and Space Science Library Vol. 285, Information Handling in Astronomy - Historical Vistas*. p. 109, doi:10.1007/0-306-48080-8_7
- Harrison E., Tadamaru E., 1975, *ApJ*, 201, 447
- Helfand D. J., Chatterjee S., Brisken W. F., Camilo F., Reynolds J., van Kerkwijk M. H., Halpern J. P., Ransom S. M., 2007, *ApJ*, 662, 1198
- Ibrahim A. I., et al., 2004, *ApJ*, 609, L21
- Jankowski F., et al., 2019, *MNRAS*, 484, 3691
- Kaspi V. M., Beloborodov A. M., 2017, *Annual Review of Astronomy and Astrophysics*, 55, 261
- Kettenis M., van Langevelde H. J., Reynolds C., Cotton B., 2006, in Gabriel C., Arviset C., Ponz D., Enrique S., eds, *Astronomical Society of the Pacific Conference Series Vol. 351, Astronomical Data Analysis Software and Systems XV*. p. 497
- Kirsten F., Vlemmings W., Campbell R. M., Kramer M., Chatterjee S., 2015, *A&A*, 577, A111
- Leahy D., 2017, *ApJ*, 837, 36
- Lobanov A. P., 1998, *A&A*, 330, 79
- Lower M., et al., 2018, *ATel*, 12288
- Lower M. E., et al., 2020, *MNRAS*, 494, 228
- Lyne A., Levin L., Stappers B., Mickaliger M., Desvignes G., Kramer M., 2018, *ATel*, 12284
- Margalit B., Beniamini P., Sridhar N., Metzger B. D., 2020, arXiv preprint arXiv:2005.05283
- Minter A. H., Camilo F., Ransom S. M., Halpern J. P., Zimmerman N., 2008, *ApJ*, 676, 1189
- Olausen S. A., Kaspi V. M., 2014, *ApJS*, 212, 6
- Pintore F., Mereghetti S., Esposito P., Turolla R., Tiengo A., Rea N., Bernardini F., Israel G. L., 2018, *MNRAS*, 483, 3832
- Putney M. L., Stinebring D. R., 2006, *Chinese Journal of Astronomy and Astrophysics*, 6, 233
- Reid M., et al., 2019, *ApJ*, 885, 131
- Rioja M. J., Dodson R., Orosz G., Imai H., Frey S., 2017, *AJ*, 153, 105
- Scholz P., et al., 2017, *ApJ*, 841, 126
- Sedov L., 1959, *Similarity and Dimensional Methods in Mechanics*
- Shan S., Zhu H., Tian W., Zhang M., Zhang H., Wu D., Yang A., 2018, *ApJS*, 238, 35
- Shepherd M. C., Pearson T. J., Taylor G. B., 1994, in *Bulletin of the American Astronomical Society*. pp 987–989
- Sokolovsky K. V., Kovalev Y. Y., Pushkarev A. B., Lobanov A. P., 2011, *A&A*, 532, A38
- Thompson C., Duncan R. C., 1995, *MNRAS*, 275, 255

APPENDIX A: MEASURING SCATTER-BROADENED SIZE OF XTE J1810–197

The angular size of a radio source can be measured from its image deconvolved by the synthesized beam. As magnetars are point-like radio sources, a non-zero deconvolved angular size of J1810 can be attributed to scatter-broadening effect caused by ISM. For each epoch, the deconvolved image of J1810 is obtained as an elliptical gaussian component; the mean of its major- and minor-axis lengths is used as the scatter-broadened size of J1810. Assuming the degree of scatter-broadening did not vary across the 14 recent epochs, the 14 measurements of scatter-broadened sizes yield a scatter-broadened size of 0.7 ± 0.4 mas for J1810.

This paper has been typeset from a $\text{\TeX}/\text{\LaTeX}$ file prepared by the author.